
Simulating Undrained Triaxial Compression Behaviour by Fluid-Coupled Distinct Element Method

Yasuhiko Okada¹⁾ and Hiroataka Ochiai²⁾

1) Department of Soil and Water Conservation, Incorporated Administrative Agency Forestry and Forest Products Research Institute, 1 Matsunosato, Tsukuba, Ibaraki 305-8687, Japan (okada10@ffpri.affrc.go.jp)

2) Department of Soil and Water Conservation, Incorporated Administrative Agency Forestry and Forest Products Research Institute, 1 Matsunosato, Tsukuba, Ibaraki 305-8687, Japan (ochi@ffpri.affrc.go.jp)

Abstract

In order to numerically reproduce the pore-pressure changes in liquefaction phenomenon, the fluid-coupled distinct element method is proposed. In this model, the dynamic changes in pore-pressure are taken into account by the changes in volumetric strain and modulus of compressibility of water in the respective measurement sphere that surrounds and coincides with each ball element. Fluid flow among the measurement spheres is controlled by Darcy's law. The numerical reproduction of shear behaviour of loose and dense sands in the triaxial compression tests under CU (consolidated undrained) conditions is performed. For the loose specimen, the pore-pressure has been monotonically increased and liquefaction has been generated at the steady state, in which normal contact force mobilized between the two elements in contact has been very small. On the other hand, the positive pore-pressure has not increased so much in the dense specimen. As the axial strain increased, the negative pore-pressure has been observed and the very large contact force between elements has been observed at the end of the test. From this result, it is concluded that our simulation model has well-reproduced the contractive and dilative behaviour of loose and dense sands by triaxial compression tests.

Keywords: fluid-coupled distinct element method, undrained triaxial compression behaviour, volumetric strain, Darcy's law, liquefaction

Introduction

Every year, the severe property damages and significant loss of life are caused by the flow-type landslides associated with the liquefaction in which excess pore-pressure generation and resulting effective normal stress and shear resistance losses are taking place. After the 1964 Niigata earthquake, the liquefaction behaviour of sands have received a great deal of attention from many researchers and the extensive geotechnical soil tests, mostly triaxial compression tests, have been conducted to reveal the triggering mechanisms (Seed and Lee 1966, Yoshimi et al. 1977, Seed 1979, Finn 1981, Ishihara et al. 1990). On the other hand, several numerical models have been proposed, in which distinct element method (DEM) by Cundall and Strack (1979) is considered one of the most effective tools for analyzing the stress-strain relationships in particulate systems, such as granular flow (Walton 1983, Kiyama 1983) and soil mechanics (Ting et al. 1989, Okura et al. 2004, Okada and Ochiai 2005).

Although the pore-pressure generation and the resulting loss of shear resistance during the landslide motion are the key for the liquefaction phenomenon, the usual DEM simulations have not taken account of the changes in pore-pressure. In this study, the numerical reproduction of the undrained triaxial compression behaviour associated with the liquefaction is challenged by the fluid-coupled DEM, in which solid-fluid interactions are taken into consideration. For the pore-pressure calculation, the concept of measurement sphere is introduced. The measurement sphere has the radius twice as much as that of the ball element and its centre coincides with the one of ball element that expresses the soil particle. Hence, each ball element is surrounded by each measurement sphere. The changes in pore-pressure are considered in the measurement sphere associated with the volumetric strains generated by the relative displacements of balls and walls intersecting the measurement sphere. The pore-pressure generations are calculated by the product of volumetric strain and the modulus of compressibility of water. The resulting differences in the pore-pressure in each measurement sphere generates the fluid flow between adjacent measurement spheres, in which Darcy's law with bulk permeability governs in our simulation.

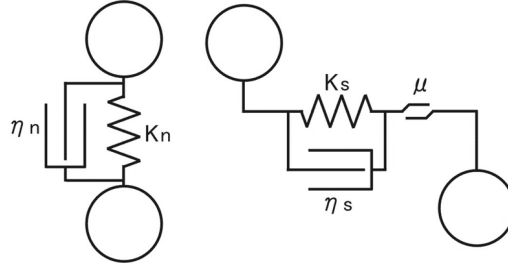


Fig. 1. Force transmission system. Elastic spring, local viscous damper, and slider assumed for contact.

Method

In fluid-coupled DEM, the contacts between ball-ball (or ball-wall) are modeled. As shown in Fig. 1, the forces acting are transmitted in normal and tangential directions. The mechanical element of elastic spring and viscous local damper are set in the normal direction, and in the tangential direction also the slider is considered. The position- and angular velocity-vectors of ball A are expressed as following:

$$[x_A] = (x_{A1}, x_{A2}, x_{A3}), \text{ and } [\omega_A] = (\omega_{A1}, \omega_{A2}, \omega_{A3})$$

Given that the position and angular velocity of ball B are expressed by the same way, the judgment of contacts between two balls is expressed as following:

$$\langle L_{AB} \rangle = \sqrt{(x_{A1} - x_{B1})^2 + (x_{A2} - x_{B2})^2 + (x_{A3} - x_{B3})^2} \leq r_A + r_B$$

in which r_A and r_B are the radius of ball A and B. The normal unit vector from the centre of ball A to B is expressed as:

$$[n_i] = ([x_{Bi}] - [x_{Ai}]) / \langle L_{AB} \rangle \quad (i = 1, 2, 3)$$

The force by elastic spring is divided into normal and tangential directions like:

$$[E_i] = ([E_i^n] - [E_i^s]) \quad (i = 1, 2, 3)$$

The force by elastic spring in normal direction is proportional to the amount of intersection of two balls as:

$$[E_i^n] = K^n \langle U^n \rangle [n_i] \quad (i = 1, 2, 3), \text{ here } \langle U^n \rangle = r_A + r_B - \langle L_{AB} \rangle$$

The contact point between two balls is as follows:

$$\langle x_i^{(c)} \rangle = [x_{Ai}] + (r_A - \langle U^n \rangle / 2) [n_i] \quad (i = 1, 2, 3)$$

The force by elastic spring in tangential direction is computed in an incremental fashion. The relative motion of contact (which is defined as the velocity of ball B relative to ball A) is given by:

$$[\nu_i] = [\dot{x}_{Bi}^{(c)}] - [\dot{x}_{Ai}^{(c)}] = \{[\dot{x}_{Bi}] + \varepsilon_{ijk} [\omega_{Bj}] ([x_k^{(c)}] - [x_{Bk}])\} - \{[\dot{x}_{Ai}] + \varepsilon_{ijk} [\omega_{Aj}] ([x_k^{(c)}] - [x_{Ak}])\}$$

$$(i = 1, 2, 3)$$

in which ε_{ijk} is Eddington's epsilon and Einstein's summation convention is applied on subscript of j and k . The relative motion is also divided into normal and tangential directions. The relative motion in tangential direction is as follows:

$$[\nu_i^s] = [\nu_i] - [\nu_i^n] = [\nu_i] - [\nu_j] \cdot [n_j] [n_i] \quad (i = 1, 2, 3)$$

The incremental displacement in tangential direction is given by:

$$[\Delta U_i^s] = [\hat{\nu}_i^s] \cdot \Delta t \quad (i = 1, 2, 3)$$

Hence, the contact force in tangential direction due to this incremental displacement is as:

$$[\Delta E_i^s] = k^s [\Delta U_i^s] \quad (i = 1, 2, 3)$$

The additional force due to the changes in contact point during Δt is approximated by:

$$[E_i^s] = \{ [E_m^s]_{old} (\delta_{lm} - \varepsilon_{lmn} \varepsilon_{npq} [n_p]_{old} [n_q]) \}_j^s \{ \delta_{ij} - \varepsilon_{ijk} [\tilde{\omega}_k] \Delta t \}$$

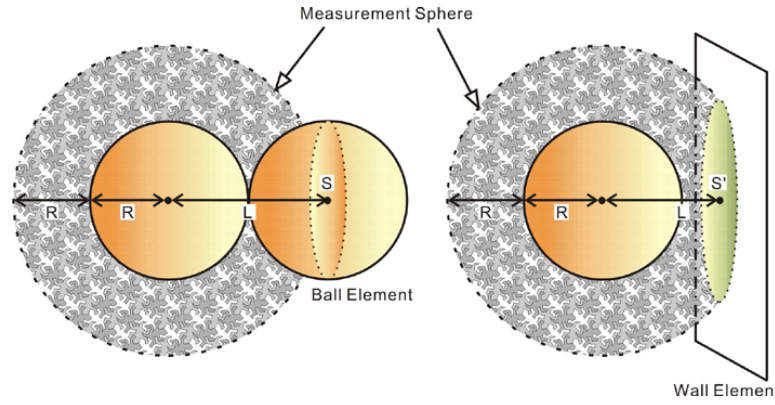


Fig. 2. The conceptual illustration of measurement sphere and the cross section areas for applying the generated pore-pressure.

where δ is Kronecher’s Delta, the subscript “old” signifies the values at the previous time-step, that is before the update, and $[\tilde{\omega}_k]$ is the average of angular velocity of ball A and B in the normal unit vector.

$$[\tilde{\omega}_i] = \frac{1}{2}(\omega_{Aj} + \omega_{Bj})n_jn_i \quad (i = 1, 2, 3)$$

Finally, the contact force by elastic spring in tangential direction is as follows:

$$[E_i^s] = [E_i^{\prime s}] + [\Delta E_i^s] \quad (i = 1, 2, 3)$$

If contact force in tangential direction surpasses the frictional force ($\mu[E_i^n]$), the force in tangential direction is set at ($\mu[E_i^n]$). The viscous local damping is introduced based on Cundall (1987) as following:

$$[D_i] = -\alpha|[E_i]| \times \text{sign}([\dot{x}_i])$$

$$\text{sign}(z) = \begin{cases} +1, & \text{if } z > 0; \\ -1, & \text{if } z < 0; \\ 0, & \text{if } z = 0. \end{cases} \text{ and}$$

in which α is damping constant and it is set at 0.7 in this study.

Then, the calculation scheme of the changes in pore-pressure associated with volumetric strain are mentioned. As shown in Fig. 2, the measurement sphere is introduced. Each measurement sphere surrounds and coincides with the centre of each ball element with the radius of “R.” The radius of measurement sphere itself is twice as large as the one of ball element, that is “2R.” The mean velocity and centre position of ball and wall elements which intersect a given measurement sphere is calculated as following:

$$\bar{\nu}_i = \sum_N \nu_i / N, \bar{x}_i = \sum_N x_i / N, \quad (i = 1, 2, 3)$$

in which N is the total number of ball and wall elements contained in the measurement sphere, ν_i is translational velocity, and x_i is centroid location of ball and wall elements. The relative velocity and position of ball and wall elements from the mean values are given by:

$$\tilde{\nu}_i = \nu_i - \bar{\nu}_i, \tilde{x}_i = x_i - \bar{x}_i \quad (i = 1, 2, 3)$$

In this model, the relative velocity is estimated by using strain rate tensor ($\dot{\beta}_{ij}$) expressed as:

$$\tilde{\nu}'_i = \dot{\beta}_{ij}\tilde{x}_j \quad (i = 1, 2, 3)$$

The strain rate tensor ($\dot{\beta}_{ij}$) that minimizes the difference between relative velocity ($\tilde{\nu}_i$) and the estimated relative velocity ($\tilde{\nu}'_i$) is computed using the least-square method, in which the following nine equations are resolved. In this calculation, LU decomposition based on the Crout’s algorithm and backward- and forward substitution were conducted.

$$\sum_N \dot{\beta}_{ij}\tilde{x}_k\tilde{x}_j = \sum_N \tilde{\nu}_i\tilde{x}_j \quad (i, j = 1, 2, 3)$$

Table 1. Parameters for simulations

Parameter	V	alue
Normal spring stiffness, K^n		$5.0 \cdot 10^{6.5} \text{ N/m}$
Shear spring stiffness, k^s		$5.0 \cdot 10^{6.5}/2 \text{ N/m}$
Frictional coefficient,		0.60
Confining pressure, σ_3	2.0	10^4 Pa
Modulus of compressibility of water		$2.0 \cdot 10^{6.5} \text{ Pa}$
Axial loading speed		0.01 m/s
Bulk permeability		$1.0 \cdot 10^{-3} \text{ m/s}$

The volumetric strain during the increment of time Δt is obtained like:

$$\varepsilon_\nu = \dot{\varepsilon}_\nu \Delta t = (\dot{\beta}_{11} + \dot{\beta}_{22} + \dot{\beta}_{33}) \Delta t$$

The changes in pore-pressure due to the volume change is given by the product of volumetric strain and the modulus of compressibility of water, and it is applied as forces to the centers of ball and wall elements which are within a measurement sphere as following:

$$\begin{aligned} F_{ball} &= P'_A S = (P_A + \Delta P) S = (P_A + E_\nu \varepsilon_\nu) \pi r^2 \\ F_{wall} &= P'_A S' = (P_A + \Delta P) S' = (P_A + E_\nu \varepsilon_\nu) \pi \{(2R)^2 - L^2\} \end{aligned}$$

in which ΔP is changes in pore-pressure within Δt , S and S' are the areas on which pore-pressure acts (Fig. 2), E_ν is the modulus of compressibility of water. The fluid flow is given based on the Darcy's law by:

$$\Delta Q_{AB} = k \cdot \pi r^2 \cdot \Delta t \cdot (P'_B - P'_A) / \rho \cdot g \cdot L_{AB}$$

where P'_A and P'_B is the pore-pressure of measurement sphere A and B, and g is the gravitational acceleration. The total changes in pore-pressure due to fluid flow (P_A) is given by:

$$P_A = \sum_N \Delta P_{AB} = \sum_N E_\nu \Delta Q_{AB} / V_A$$

Finally, the equations of trnaslational and rotational motion are as following:

$$m_A [\ddot{x}_{Ai}]_t = -[E_i]_t + [D_i]_t - [F_i]_t - m_A [g_i], I[\ddot{\omega}_{Ai}]_t = -\varepsilon_{ijk} ([x_j^{(c)}]_t - [x_{Aj}]_t) ([E_k]_t + [D_k]_t)$$

By integrating these equations, velocity, position, and angular velocity are calculated as:

$$[\dot{x}_{Ai}]_{t+\Delta t/2} = [\dot{x}_{Ai}]_{t-\Delta t/2} + [\ddot{x}_{Ai}]_t \cdot \Delta t, [x_{Ai}]_{t+\Delta t} = [x_{Ai}]_t + [\dot{x}_{Ai}]_{t+\Delta t/2} \cdot \Delta t, [\omega_{Ai}]_{t+\Delta t/2} = [\omega_{Ai}]_{t-\Delta t/2} + [\dot{\omega}_{Ai}]_t \cdot \Delta t.$$

The values of $m_A [\ddot{x}_{Ai}]_{t+\Delta t}$ and $I[\ddot{\omega}_{Ai}]_{t+\Delta t}$ are calculated by repeating the procedures mentioned above.

Triaxial compression test simulation and results

The cylindrical-shape specimens with the diameter at 0.05 m and the height at 0.1 m were created for the undrained triaxial compression test simulation (Fig. 3). The ball elements were set at the diameter of 0.01 m and the density of $2,570 \text{ kg/m}^3$. The value of bulk compressibility of water in this study was set at $2.3 \times 10^{6.5} \text{ Pa}$ in consideration of the mixture of air inside the water. Frictional coefficients of ball and wall element were set at 0.6, that is equivalent to the friction angle of 31 degrees. The bulk permeability in the cylindrical specimen was given at $1.0 \times 10^{-3} \text{ m/s}$. The loose and dense specimens at the void ratios (e_0) of 1.03 and 0.8 at the initial consolidation of 20 kPa were formed. The mechanical constants and calculation conditions for the numerical simulation are summarized in Table 1.

Fig. 4 shows the generalized image of the triaxial compression test results on the loose and dense specimens of sand, in which 4(a) shows the effective stress paths and 4(b) illustrates the relationship of pore-pressure versus axial strain. For the loose specimen, pore-pressure is monotonically increased associated with the tendency of contractive volumetric strain, where effective stress path is going left suffering from small deviator stress. The liquefaction-related disasters are to be controlled by this kind of soil behaviour, in which

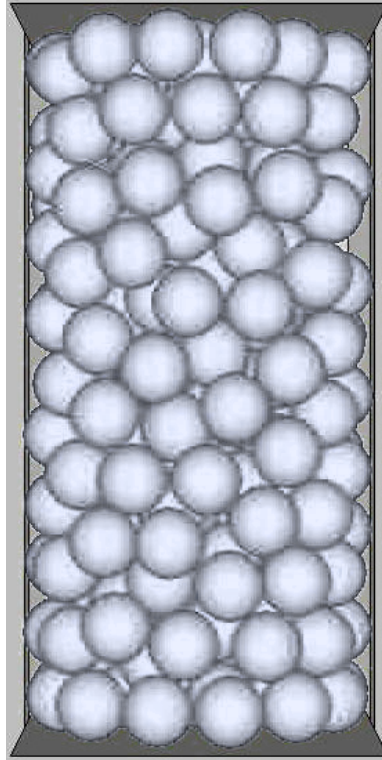


Fig. 3. The numerical specimen at the initial consolidation for triaxial compression test.

the soil particles are almost floated in the water and behave resembling the viscous liquid. On the other hand, pore-pressure is not increased, but sometimes decreased, in the densely packed specimen, in which effective stress path is going right-upward, resulting in the high deviator stress.

The effective stress paths of loose and dense specimens modeled for our numerical simulation are illustrated in Fig. 5. The effective stress path of loose specimen ($e_0 = 1.03$) moved toward left and the final stress point showed the only 5 kPa in effective mean stress. Whereas, the effective stress path of dense specimen ($e_0 = 0.80$) climbed rightward, where the effective mean stress as much as 130 kPa was mobilized at the end of the test. Fig. 6 shows the relationship between pore-pressure versus axial strain. For the loose specimen, the pore-pressure mostly increased at the initial axial strain ranged until 1.0 % likely accompanied by the considerable contractive changes in volumetric strain. After the initial increase in pore pressure, the pressure remained almost constant at a value equivalent to the confining pressure indicating that the specimen liquefied. On the other hand, the pore-pressure in the dense specimen showed the negative values as the compression proceeded. At this time, the expansive volumetric changes were observed. It means that the ball elements rolled over the others when they changed their positions during the test, resulting in the dilation.

The normal contact forces acting between the ball and wall elements after the numerical triaxial compression simulation on loose and dense specimens are shown in Fig. 7. As for the dense specimen, the contact forces were acting in the whole specimen and the strong chains in axial direction were particularly observed. The maximum contact force at the end of the test was 87.7 N. Whereas, the only dispersive contact forces were mobilized due to the increase of pore-pressure in the loose specimen, especially among the middle part of the cylindrical-shaped model. The maximum contact force was 2.6 N. The maximum contact force of dense specimen was about 33 times as much as the one of loose specimen. These behaviours in stress and pore-pressure — strain relationship of loose and dense specimens resembled those found in the general triaxial compression tests above-illustrated in Fig. 4.

Conclusions

The fluid-coupled distinct element method was proposed to numerically reproduce the undrained triaxial compression behaviour that was directly associated with the liquefaction-related disasters, in which pore-pressure were calculated in the measurement spheres. The scheme of the pore-pressure estimation by the volumetric change and the modulus of compressibility of water was investigated and the followings were

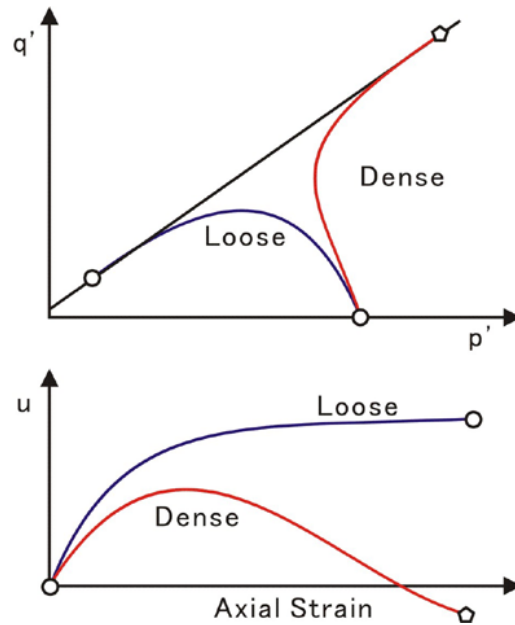


Fig. 4. The generalized image of the triaxial compression tests results. (a) Effective stress paths. (b) changes in pore-pressure.

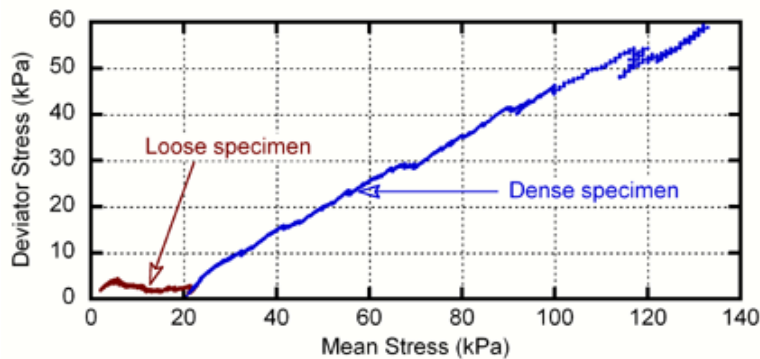


Fig. 5. Effective stress paths obtained from numerical simulation.

drawn:

1. The rise in the pore-pressure and the small normal contact forces between ball and wall elements were reproduced in the loose specimen, which could explain the generation of liquefaction phenomenon; and
2. The strong contact forces between ball and wall elements forming the stable chains in axial direction were mobilized in the dense specimen simulation. The negative pore-pressure and expansive volumetric strain were recorded as the compression proceeded, which adequately reproduce the dilative shear behaviour usually found in the general triaxial compression test on dense sand.

References

- Cundall, P.A. and Strack, O.D.L. (1979) A discrete numerical model for granular assemblies. *Géotechnique*, **29**(1), pp. 47–65.
- Finn, W.D.L. (1981) Liquefaction potential: developments since 1976. In *Proceedings of the 1st International Conference on Recent Advances in Geotechnical Earthquake Engineering and Soil Dynamics*. St. Louis, Mo., 26 April–3 May 1976. University of Missouri-Rolla, Rolla, Mo. **2**, pp. 655–681.
- Ishihara, K., Okusa, S., Oyagi, N., and Ischuk, A. (1990) Liquefaction-induced flowslide in the collapsible loess deposit in Soviet Tajik. *Soils and Foundations*, **30**(4), pp. 73–89.

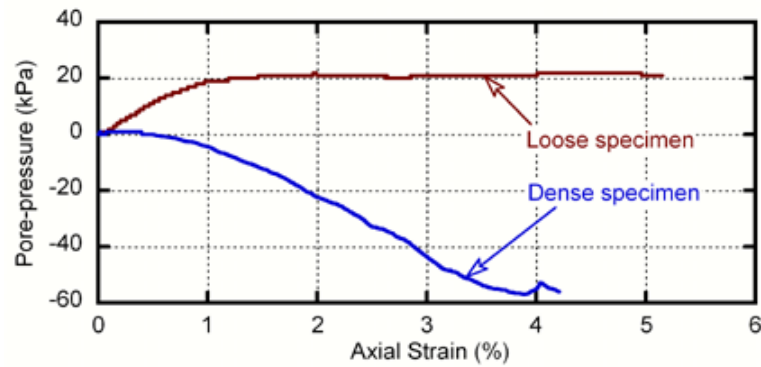


Fig. 6. Relationship between pore-pressure and axial strain found in the numerical simulation.

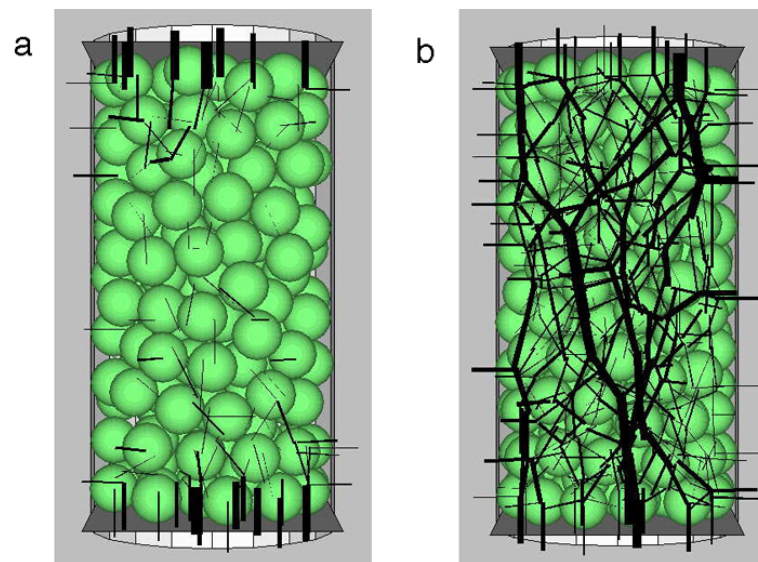


Fig. 7. The contact forces acting on the particles at the end of the tests. (a) loose specimen. (b) dense specimen.

- Kiyama, H., and Fujimura, H. (1983) Application of Cundall's discrete block method to gravity flow analysis of rock-like granular materials. In Proceedings of the Japan Society of Civil Engineers. **333**, pp. 137–146.
- Okada, Y., and Ochiai, H. (2005) Fluid-coupled DEM modeling for the undrained shear behaviour of sands. In Proceedings of the 44th meeting of the Japan Landslide Society. 1, pp. 146–146.
- Okura, Y. Ochiai, H., Cundall, P.A., and Shimizu, Y. (2004) Fluid coupling in PFC^{3D} using the measurement spheres. In Proceedings of the 2nd International PFC Symposium, "Numerical Modeling in Micromechanics via Particle Method — 2004." Kyoto, Japan, 28–29 October 2004. A.A. Balkema, Leiden, The Netherlands. 1, pp. 257–264.
- Seed, H.B. 1979 Soil liquefaction and cyclic mobility evaluation for level ground during earthquakes. Journal of the Geotechnical Engineering Division, ASCE. **105**, pp. 201–255.
- Seed, H.B., and Lee, K.L. 1966 Liquefaction of saturated sand during cyclic loading. Journal of the Soil Mechanics and Foundations Division, ASCE. **92**(CM6), pp. 105–134.
- Ting, J.M., Corkum, B.T., Kauffman, C.R., and Creco, C. (1989) Discrete numerical model for soil mechanics. Journal of the Geotechnical Engineering Division, ASCE. **115**(3), pp. 379–398.
- Walton, O.R. (1983) Particle-dynamics calculations of shear flow. In "Mechanics of Granular Materials." Elsevier Science, Amsterdam, The Netherlands. pp. 327–338.
- Yoshimi, Y., Richart, F.E., Prakash, S., Balkan, D.D., and Ilyichev, V.A. 1977 Soil dynamics and its application to foundation engineering. In proceedings of 9th International Conference on Soil Mechanics and Foundation Engineering, Tokyo, Japan, 11–15 July 1977. A.A. Balkema, Rotterdam, The Netherlands. **2**, pp. 605–650.